# MEMS, Field-Emitter, Thermal, and Fluidic Devices

# Development of a Tabletop Deep Reactive-Ion Etching System for MEMS Development and Production

P. A. Gould, M. D. Hsing, K. K. Gleason, M. A. Schmidt
Sponsorship: MTL

A general rule of thumb for new semiconductor fabrication facilities (fabs) is that revenues from the first year of production must match the capital cost of building the fab itself. With modern fabs routinely exceeding $1 billion to build, this rule serves as a significant barrier to entry for research and development and groups seeking to commercialize new semiconductor devices aimed at smaller market segments that require a dedicated process. To eliminate this cost barrier, we are working to create a suite of tools that will process small (~1") substrates and cost less than $1 million. This suite of tools, known colloquially as the 1" Fab, offers many advantages over traditional fabs. By shrinking the size of the substrate, we trade off high throughputs for significant capital cost savings while incurring substantial savings in material usage and energy consumption. This substantial reduction in the capital cost will drastically increase the availability of semiconductor fabrication technology and enable experimentation, prototyping, and small-scale production to occur locally and economically. To implement this suite of 1" Fab tools, our current research has been focused primarily on developing a deep reactive-ion etching (DRIE) system. DRIE tools are used to create highly anisotropic, high aspect-ratio trenches in silicon—a crucial element in many MEMS processes that will benefit from a 1" Fab platform. A labeled image of the 1" Fab DRIE system is shown in Figure 1. The load lock and wafer lift assembly allow up to 2" wafers and pieces to be easily loaded and processed, and the modularized design of the processing chamber means that the (currently DRIE) system can be easily adapted to produce other plasma-based etching and deposition tools (such as PECVD and RIE). Using the switched-mode Bosch Process, the 1" Fab DRIE system currently can achieve silicon etch rates up to 6 μm/min with vertical sidewall profiles, an estimated photoresist selectivity greater than 75:1, and etch depth non-uniformity to less than 2% across the substrate. Several examples of anisotropic etches performed with our system are included in Figure 2. Presently, we are working to refine the thermal design of the system and optimize recipes for high-aspect ratio etching.

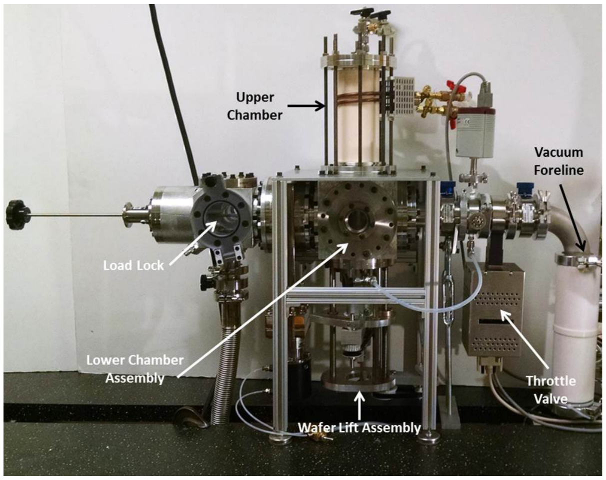

▲Figure 1: View of the basic components of the 1" Fab DRIE system.

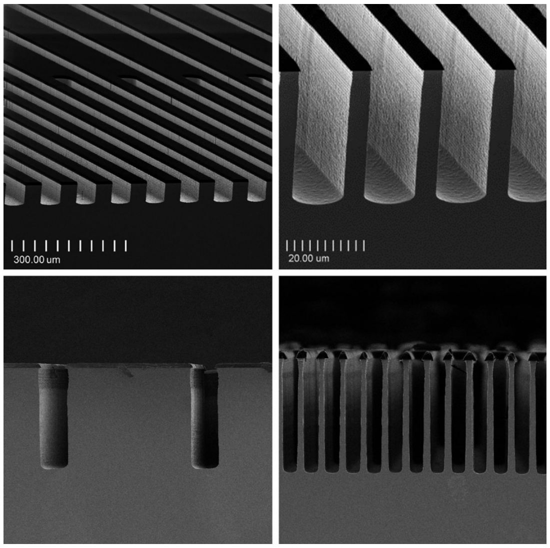

▲Figure 2: Examples of anisotropic etches performed using the Bosch process in the 1" Fab DRIE.

## FURTHER READING

- S. Heck, S. Kaza, and D. Pinner. (2011, Autumn) "Creating Value in the Semiconductor Industry" [Online]. Available: http://www.mckinsey.com/~/media/McKinsey/dotcom/client_service/Semiconductors/PDFs/MOSC_1_Value_creation.ashx.
- P. A. Gould, M. D. Hsing, H. Q. Li, K. K. Gleason, and M. A. Schmidt, "An Ultra-low Cost Deep Reactive Ion Etching (DRIE) Tool for Flexible, Small Volume Manufacturing," *Solid-State Sensors, Actuators and Microsystems (TRANSDUCERS)*, pp. 2268-2271, 2015.

# Resonant Body Transistor with MIT Virtual Source (RBT-MVS) Compact Model

B. Bahr, D. Weinstein, L. Daniel

Sponsorship: NSF NEEDS

High-Q mechanical resonators are crucial components for filters and oscillators that are essential for RF and analog circuits. It is highly desirable for resonators to scale to GHz-frequencies and beyond to meet today's challenging requirements in terms of speed and data rates. Furthermore, aggressive scaling requirements call for monolithic integration with CMOS circuits to allow for a smaller footprint and reduced parasitics and power consumption. Micro-electromechanical (MEM) resonators represent a potential solution for frequency and footprint scaling, along with monolithic integration in CMOS.

A resonant body transistor (RBT) is a MEM resonator with a field-effect transistor (FET) incorporated into the resonator structure. The FET is intended for active sensing of the mechanical vibrations through piezoresistive modulation of the channel mobility. RBTs also rely on electrostatic internal dielectric transduction for actuation, by means of MOS capacitors (MOSCAPs). Such sensing and actuation enable these devices to easily scale to multi-GHz frequencies, while being compatible with CMOS manufacturing technologies.

Compact modeling for these devices is essential to gain a deeper insight into the tightly coupled physics of the RBT while emphasizing the effect of the different parameters on the device performance. It also grants circuit designers and system architects the ability to quickly assess the performance of prospective RBTs, while minimizing the need for computationally intensive coupled-multi-physics finite element method (FEM) simulations.

The RBT compact model is developed as a set of modules, each representing a physical phenomenon. Mechanical resonance, FET sensing, MOSCAP driving, and thermal modules are the most notable. The modules are interconnected through a set of nodes (namely, mechanical nodes and a thermal node) to represent the coupling between the different physics. This modular approach enables the seamless expansion of the RBT model either by incorporating new physics, adding driving or thermal sources, or mechanically coupling multiple RBTs together. A modified version of the MIT Virtual Source (MVS) model is used to implement both the electrostatic driving (as a MOSCAP) as well as the piezoresistive active FET sensing. The full model is developed in Verilog-A and available on nanohub.org.

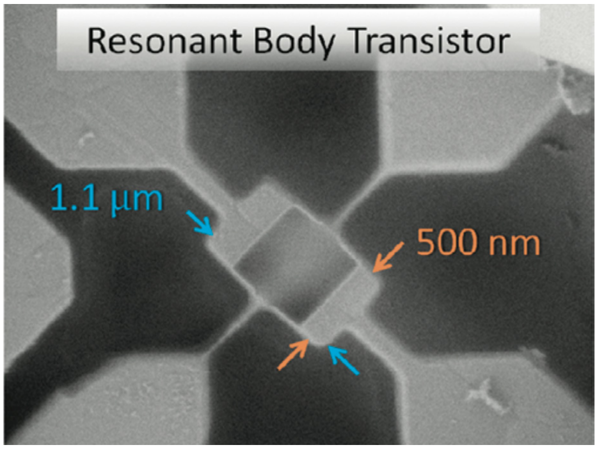

▲ Figure 1: The first RBT, developed by D. Weinstein and S. Bhave in 2009 at Cornell University.

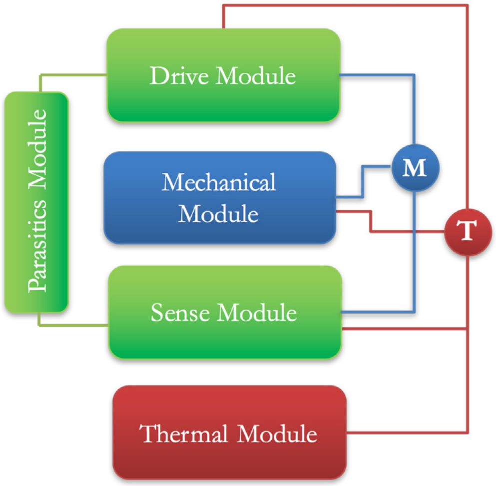

▲ Figure 2: Modular RBT model, with each physical phenomenon represented by a module. Different modules are connected through a mechanical node (M) and thermal node (T).

---

FURTHER READING

- D. Weinstein and S. Bhave, "The Resonant Body Transistor," *Nano Letters*, pp. 1234–1237, 2010.
- B. Bahr, D. Weinstein, and L. Daniel, "RBT-MVS Model" [Online]. Available: nanohub.org: https://nanohub.org/publications/72/1.
- B. Bahr, D. Weinstein, and L. Daniel, "URBT-MVS Model" [Online]. Available: nanohub.org: https://nanohub.org/publications/132/1.

# Piezoelectric Micro-Machined Ultrasonic Transducer Array for Medical Imaging

K. M. Smyth, C. G. Sodini, S.-G. Kim

Sponsorship: Medical Electronic Device Realization Center, Analog Devices, Inc.

Diagnostic medical ultrasound imaging is becoming increasingly widespread because it is relatively inexpensive, portable, compact, and non-invasive compared to other diagnostic scanning techniques. However, commercial realization of advanced imaging trends will require cost-effective, large-scale arrays of miniaturized elements, which are expensive to fabricate with the current bulk piezoelectric transducers. At high volume, micro-fabricated transducers based on micro-electro-mechanical (MEMS) technology are an array-compatible and low-cost option.

The piezoelectric micro-machined ultrasonic transducer (pMUT) is a promising alternative to previously proposed capacitive MUT devices since it does not suffer from electrostatic transduction limitations, including potentially unsafe high bias voltage, and non-linearity. With more effective transformation via the piezoelectric effect, pMUTs have already demonstrated viability for deep penetration imaging via high acoustic pressure output. However, insufficient modeling has produced pMUT devices that often fall short of predictions, resulting in low electromechanical coupling and reduced bandwidth. With an improved modelling framework and optimization, pMUT based arrays have the potential for efficient, low-power, and high-pressure operation necessary for wearable applications.

Based on a high force-output figure of merit, a 31-mode, lead zirconate titanate (PZT)-based pMUT plate cell design is selected. Our previous work developed and validated an analytical, electro-acoustic model of the single cell through experiment and finite element simulation. By leveraging and building on the validated single-cell model, we further optimized parallelized multi-cell elements to achieve high acoustic power and power efficiency. These elements are incorporated into 1D arrays (Figure 1) to demonstrate basic beamforming and image collection capabilities of a pMUT-based ultrasound system.

Current work focuses on fabrication of the pMUT arrays (Figure 2) using common micro-fabrication techniques including a PZT sol-gel deposition process. Beyond fabrication, the project aims to generate proof-of-concept images to demonstrate the commercial viability of pMUT-based array systems.

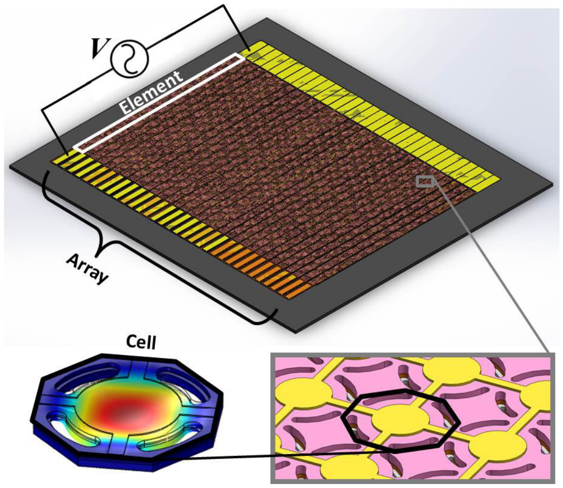

▲ Figure 1: Rendering of 1D pMUT array (top) in which each element consists of many small pMUT cells (bottom right). Deflection of single cell based on piezo-acoustic finite element model simulated in COMSOL (bottom left).

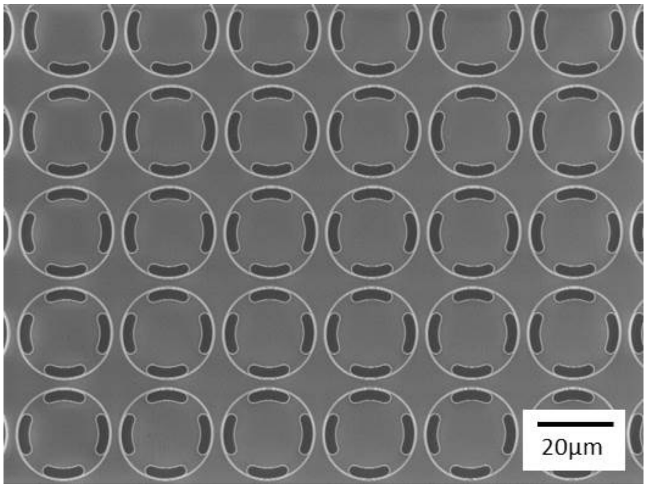

▲ Figure 2: Scanning electron microscope image of partially completed pMUT cells currently undergoing fabrication.

## FURTHER READING

- K. Smyth, S. Bathurst, F. Sammoura, and S.-G. Kim, "Analytic Solution for N-electrode Actuated Piezoelectric Disk with Application to Piezoelectric Micromachined Ultrasonic Transducers," *IEEE Trans. Ultrason. Ferroelectr. Freq. Control*, vol. 60, no. 8, pp. 1756–1767, August 2013.
- K. Smyth and S.-G. Kim, "Experiment and Simulation Validated Analytical Equivalent Circuit Model for Piezoelectric Micromachined Ultrasonic Transducers," *IEEE Trans. Ultrason. Ferroelectr. Freq. Control*, vol. 62, no. 4, pp. 744–765, April 2015.

# MEMS Energy Harvesting from Low-Frequency and Low-Amplitude Vibrations

R. Xu, S.-G. Kim
Sponsorship: MIT-SUTD International Design Center

Vibration energy harvesting at the microelectromechanical system (MEMS) scale will promisingly advance exciting applications such as wireless sensor networks and the Internet of Things by eliminating troublesome battery-changing or power wiring. On-site energy generation could be an ideal solution to powering a large number of distributed devices usually employed in these systems. To enable the envisioned battery-less systems, a fully assembled energy harvester at the size of a quarter-dollar coin should generate robustly $10^1$~$10^2$ μW of continuous power from ambient vibrations (mostly less than 100 Hz and 0.5 g acceleration) with wide bandwidth. We are inching close to this goal in terms of power density and bandwidth, but not in terms of low-frequency and low-amplitude operations.

Most reported vibration energy harvesters use a linear cantilever resonator to amplify the energy absorption from weak ambient vibrations. While such structures are easy to model, design, and build, they typically have unusably narrow bandwidths. In contrast, nonlinear resonators have a different dynamic response and greatly increase the bandwidth by hardening or softening the resonance characteristic. Our previous research with nonlinear resonating bridge-structure-based energy harvesters achieved 2.0 mW/$\text{mm}^3$ power density with >20% power bandwidth. However, they were operated with input vibrations of >1 kHz at 4 g, which practically limits the use of this technology for harvesting energy from real environmentally available vibrations. Many believed this is an inherent limitation imposed on the MEMS-scale structures.

We approached this problem with a buckled-beam-based bi-stable nonlinear oscillator. Compared to mono-stable nonlinear oscillations, we found bi-stable oscillations could bring more dynamics phenomena to help reduce the operating frequency. An electromechanical lumped model has been built to simulate the dynamics of the buckled clamped-clamped beam-based piezoelectric energy harvesters. The two oscillation modes, intra-well and inter-well with respect to the double-well energy potential of the bi-stable system, have been predicted. The characteristic spring softening and spring stiffening responses corresponding to the simulations were observed by testing a meso-scale prototype. The testing results also verify the theoretical prediction on low-frequency operation, showing a shifted response of bi-stable configuration, which generates more power than the mono-stable configuration at lower frequencies. A MEMS mechanical bi-stable oscillator has also been fabricated to verify the operating frequency and amplitude of the new design (Figure 1). The multi-layer bridge structure has employed compressive residual stress in the microfabricated thin films to induce buckling and lower the operation frequencies. The dynamic responses were measured by a laser Doppler vibrometer (Figure 2). The wide-band nonlinear response shows a one-order-of-magnitude lower frequency range at low g's. The fully functional piezoelectric devices are under fabrication.

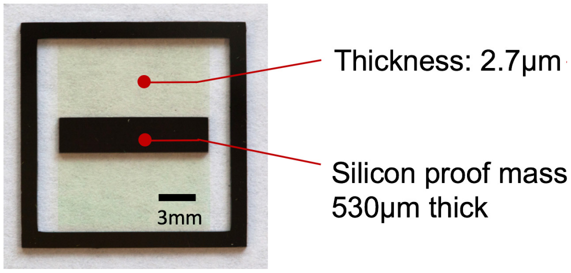

▲Figure 1: Top view of the fabricated MEMS prototype (the aspect ratio of the clamped-clamped plate is 4444:1). The plate vibrates out-of-plane during excitation.

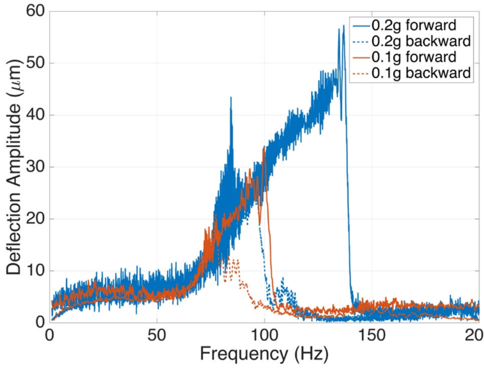

▲Figure 2: Frequency response of the MEMS prototype. The tilted peak shows the spring stiffening response with a wide bandwidth. The tests were done at 0.1g and 0.2g.

## FURTHER READING

- R. Xu and S.-G. Kim, "MEMS Energy Harvesting from Low-frequency and Low-g Vibrations," *2015 MRS Spring Meeting*, San Francisco, CA, 2015.
- R. Xu and S.-G. Kim, "Low-Frequency, Low-G MEMS Piezoelectric Energy Harvester," *PowerMEMS 2015*, Boston, MA, 2015.

# Wearable Energy Harvesters Based on Aligned Mats of Electrospun Piezoelectric Nanofibers

D. Olvera-Trejo, L. F. Velásquez-García
Sponsorship: U.S. Army

Battery recharging and replacement are still challenging after several decades of developing energy sources for portable and wireless devices. For this reason, new power sources have become essential for current and future stand-alone devices. Energy harvesters are an attractive alternative for supplying power in these systems.

We are developing wearable energy harvesters based on electrospun piezoelectric nanofibers as transducing elements. The proposed harvesting device consists of a set of flexible interdigitated electrodes on a flexible substrate; the electrodes are coated with aligned piezoelectric nanofibers. Each time the substrate is stretched or bent, the piezoelectric nanofibers produce voltage and charge that can be used to feed low-power devices. Our energy harvesters could be integrated into garments, allowing people to carry less weight and volume in batteries, which is particularly advantageous on long journeys and when located far from the electrical grid.

The piezoelectric nanofibers of our energy harvester are made of poly(vinylidene difluoride), i.e., PVDF, using the electrospinning technique. In electrospinning, a solution rich in long-chain polymers that is subject to a high electrostatic field ejects a jet that is thinned to a submicron diameter due to the interaction of the electric field and surface tension effects on the fiber (Figure 1). Highly aligned fiber deposition on the interdigitated electrodes of the energy harvester is necessary to achieve high efficiency. With this goal in mind, we developed a custom rotating collector system that allows control of the alignment and diameter of the deposited nanofibers. The collected fibers tend to be more aligned and exhibit smaller fiber diameters when the collector drum rotates at thousands of revolutions per minute (Figure 2). Current work focuses on controlling the morphology of the PVDF fibers and nanofiber mats, as well as on testing nanofiber harvester prototypes using a custom apparatus and benchtop electronics.

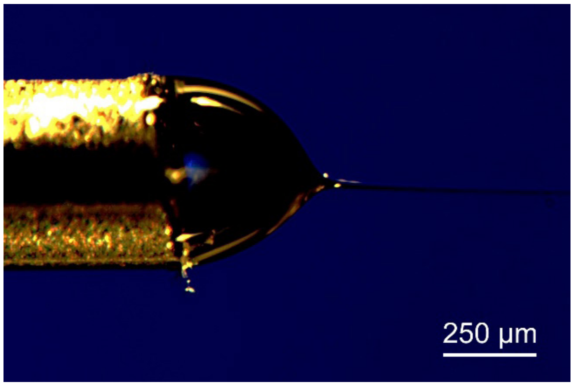

▲Figure 1: Electrospinning emitter in operation. A fine jet of liquid is electrohydrodynamically ejected from the emitter tip due to the high electric fields present there; the jet is stretched into a nanofiber due to the surface tension and electrostatic forces it experiments while traveling to the collector electrode.

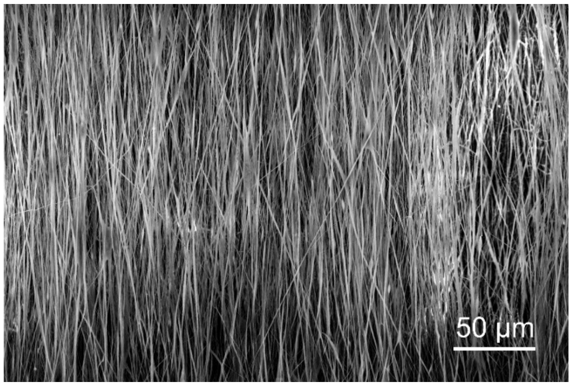

▲Figure 2: SEM micrograph of aligned PVDF nanofibers deposited on a rotating drum collector.

## FURTHER READING

- P. J. Ponce de Leon, F. A. Hill, E. V. Heubel, and L. F. Velásquez-García, "Parallel Nanomanufacturing via Electrohydrodynamic Jetting from Microfabricated Externally-fed Emitter Arrays," *Nanotechnology*, vol. 26, no. 22, pp. 225301, June 2015.

# Thin, Flexible, and Stretchable Tactile Sensor Based on a Deformable Microwave Transmission Line

M. E. D'Asaro, D. B. Sheen, J. H. Lang
Sponsorship: NSF CSNE

Over the past decade, there have been numerous publications on tactile sensors and skins aimed at replicating the human sense of touch in applications such as robotics, healthcare, and prosthetics. A variety of technologies are used, with the dominant ones being piezoresistive and capacitive, but both of these technologies have limitations due to mechanical fragility, complex fabrication, and the need for large numbers of connections to external electronics. We have developed another sensing technology that is mechanically robust, simple to fabricate, and requires only one connection to external electronics.

The new sensor, shown in Figure 1, consists of a flexible and stretchable 1.6-mm-thick microstrip transmission line with conductors made of stretchable silver-based conductive cloth and a dielectric made of soft silicone rubber (PDMS). When pressure is applied to the line, the dielectric is deformed, causing a local impedance discontinuity in the line. We have developed an algorithm that can reconstruct the deformation of the line as a function of position, based on the measured impedance of the line across a wide frequency range (30 MHz to 6 GHz).

To characterize the sensor and algorithm, the sensor was precisely deformed using a custom-designed jig based on a micrometer head while its impedance was measured in real time with a vector network analyzer. The analyzer was connected to a computer. in which the output was processed to display a plot of the reconstructed deformation, also in real time. To correct for imperfections in fabrication, any deformation present with the sensor at rest was subtracted from the responses with pressure applied. Three different pressures were applied at each of three locations, and the responses were combined to create Figure 2. Note that the reconstruction algorithm is derived entirely from physical theory and was calibrated to the measured velocity factor of the line but was not otherwise tuned to match the individual device.

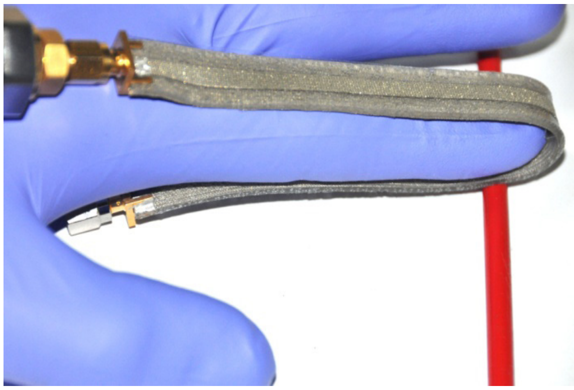

▲ Figure 1: Sensor, mounted on nitrile glove. The sensor is flexible, stretchable, and rugged and is fabricated from silver cloth and silicone rubber.

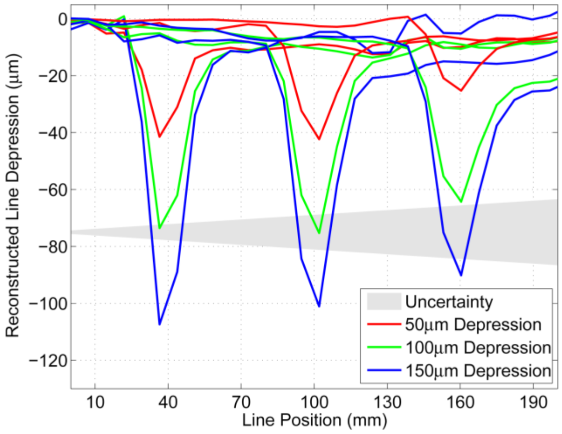

▲ Figure 2: Response of the sensor to depressions applied at 40 mm, 100 mm, and 160 mm. The sensor is accurate in position to within a single data point (7.3 mm) and in depression to within 30% at 40 mm.

## FURTHER READING

- M. E. D'Asaro, D. B. Sheen, and J. H. Lang, "Thin Flexible and Stretchable Tactile Sensor Based on a Deformable Microwave Transmission Line," *Hilton Head 2016 Workshop on Solid-State Sensors, Actuators and Microsystems*, June 2016.
- C. Lucarotti, C. M. Oddo, N. Vitiello, and M. C. Carrozzo, "Synthetic and Bio-Artificial Tactile Sensing: A Review," *Sensors*, vol. 13, no. 2, pp. 1435-1466, January 2013.
- M. L. Hammock, A. Chortos, B. C.-K. Tee, J. B.-H. Tok, and Z. Bao, "25th Anniversary Article: The Evolution of Electronic Skin (E-Skin): A Brief History, Design Considerations, and Recent Progress," *Advanced Materials*, vol. 25, no. 42, pp. 5997-6038, October 2013.

# Close-Packed Silicon Microelectrodes for Scalable Spatially Oversampled Neural Recording

J. Scholvin, J. P. Kinney, J. G. Bernstein, C. Moore-Kochlacs, N. Kopell, C. G. Fonstad, E. S. Boyden
Sponsorship: Simons Center for the Social Brain at MIT, Paul Allen Family Foundation, NYSCF, NIH, NSF

The extracellular recording of brain activity in the mammalian brain provides an important tool for understanding neural codes and brain dynamics. Extracellular electrodes with recording sites that are closely packed can enable spatial oversampling of neural activity, which facilitates data analysis; such oversampling becomes important when we aim to scale up the number of neurons used for recording.

We designed and implemented close-packed silicon microelectrodes (Figure 1) to enable the spatially oversampled recording of neural activity (Figure 2) in a scalable fashion, using a tight continuum of recording sites along the length of the recording shank, rather than discrete arrangements of tetrode-style pads or widely spaced sites. This arrangement, thus, enables spatial oversampling continuously running down the shank, so that sorting of spikes recorded by the densely packed electrodes can be facilitated for all the sites of the probe simultaneously.

We use MEMS microfabrication techniques to create thin recording shanks, and a hybrid lithography process that allows a dense array of recording sites, which we connect with submicron dimension wiring. We have performed neural recordings with our probes in the live mammalian brain. Figure 2 illustrates the spatial oversampling potential of close packed electrode sites.

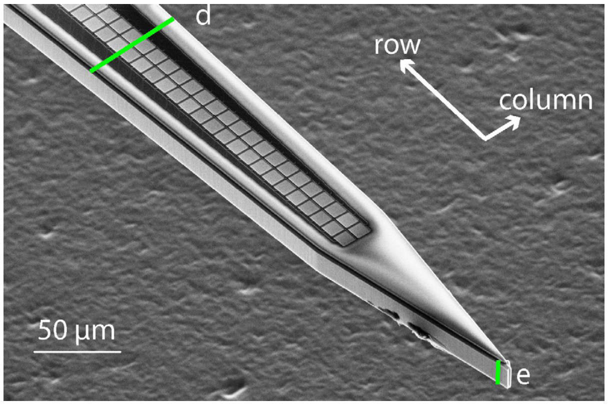

▲ Figure 1: Close-up of the tip section of a recording shank, showing the two columns and a dense set of rows. The close packed pads are visible as light squares in the center of the shank. Insulated metal wires connect to individual sites, running next to recording sites along length of shank and visible as dark lines flanking rows of light squares. The shank itself is ~50-60 µm wide (d) and 15 µm thick (e) in the regions shown.

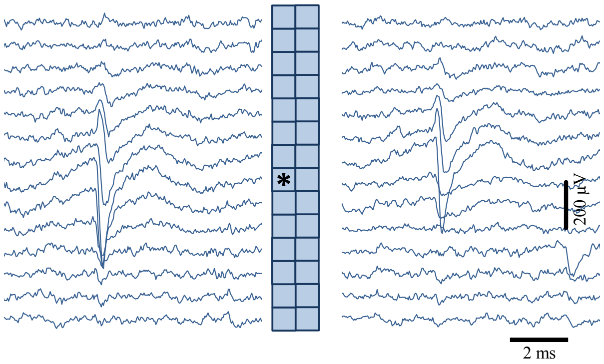

▲ Figure 2: *In vivo* recorded data for a single spike across 28 pads (2 columns by 14 rows). The spatial oversampling enables the spike to be picked up by many nearby recording sites (9 x 9 µm pads, at a 10.5 µm pitch), to facilitate automated data analysis.

## FURTHER READING

- J. Scholvin, J. P. Kinney, J. G. Bernstein, C. Moore-Kochlacs, N. Kopell, C. G. Fonstad, and E. S. Boyden, "Close-Packed Silicon Microelectrodes for Scalable Spatially Oversampled Neural Recording," *IEEE Trans. Biomed. Eng.*, vol. 63, no. 1, pp. 120–130, 2016.
- B. D. Allen, C. Moore-Kochlacs, J. Scholvin, J. P. Kinney, J. G. Bernstein, S. B. Kodandaramaiah, N. J. Kopell, and E. S. Boyden, "Towards Ground Truth in Ultra-dense Neural Recording," in *Computational and Systems Neuroscience (Cosyne)*, 2016.

# Extreme Heat Flux Thermal Management via Thin-film Evaporation

S. Adera, D. S. Antao, R. Raj, E. N. Wang

Sponsorship: ONR, NSF GRFP

Thermal management is a primary design concern for numerous power-dense equipment such as power amplifiers, solar energy convertors, and advanced military avionics. During operation, these devices generate large amounts of waste heat (>1 kW/cm$^2$) from sub-millimeter areas. These concentrated heat loads are spatially and temporally non-uniform and cause hotspots which are localized regions with extreme heat flux and exceedingly high temperature that can adversely impact device performance and reliability.

In this study, we demonstrate an extreme heat flux thermal management solution targeted towards cooling hotspots. Our test devices utilize well-defined silicon micropillar arrays which were fabricated via contact photolithography and deep-reactive-ion-etching for passive fluidic transport (i.e., capillary-wicking). Resistive thin-film heaters were integrated on the back side of our test device via electron-beam evaporation and acetone lift-off to emulate the heat generated by actual electronic chips during operation. The heaters which were used to measure temperature in addition to providing heating were calibrated prior to experiments in a convection oven. The hotspots (640×620 μm$^2$) were spatially distributed over the microstructured surface (1×1 cm$^2$). Uniform background heating was provided by heating the entire microstructured surface using a 1×1 cm$^2$ thin-film heater. Experiments were conducted in a temperature-controlled stainless steel environmental chamber which was maintained at saturated temperature and the corresponding pressure.

We dissipated ≈6 kW/cm$^2$ from a single hotspot without background heating before the microstructured surface dried out (Figure 1a). Dryout occurs due to liquid starvation when the viscous losses exceed the capillary pressure generated owing to the meniscus shape. We activated concurrent hotspots on our test devices over the 1×1 cm$^2$ microstructured surface and examined the hotspot dryout heat flux. Our experiments show that this hotspot dryout heat flux decreased monotonically when concurrent hotspots were present on the microstructured surface (left ordinate, Figure 1b). The dryout heat flux, which was ≈6 kW/cm$^2$ when a single hotspot (H2) was present, decreased to ≈4 kW/cm$^2$ per heater when two hotspots (H1/H3) were present (left ordinate, Figure 1b). This dryout heat flux decreased further to ≈3 kW/cm$^2$ per heater when three hotspots (H1/H2/H3) were present (left ordinate, Figure 1b). When a 10 W/cm$^2$ and 20 W/cm$^2$ uniform background heating was superposed with a hotspot, the hotspot dryout heat flux, which was ≈6 kW/cm$^2$ without background heating, decreased to ≈4 kW/cm$^2$ and ≈3 kW/cm$^2$, respectively (left ordinate, Figure 1c). Despite the decrease in the hotspot dryout heat flux, the total heating power increased when concurrent hotspots were created (right ordinate, Figure 1b) or when uniform background heating was superposed with a hotspot (right ordinate, Figure 1c). Our experiments show that thin-film evaporation is a promising thermal management solution for the next generation of power amplifiers and radio-frequency devices which generate extreme heat fluxes in excess of 1 kW/cm$^2$. The insights gained from this study can be used to improve the design of wicking structures which are commonly used in phase-change-based thermal management devices such as heat pipes and vapor chambers.

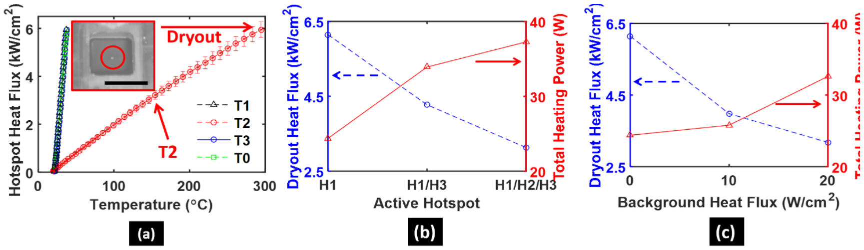

◀ Figure 1: (a) Heat flux as a function of temperature as measured by the different sensors (H1, H2, H3, and H0). A dry island formed at the hotspot H2 (inset, scale bar = 10 mm) when viscous losses exceed capillary pressure. Hotspot temperature (T2) was measured at the location where the heat was generated using heater H2. Local temperatures 3 mm away from the hotspot (T1 and T3) were measured using H1 and H3. Background temperature (T0) which is the average temperature of the entire 1×1 cm$^2$ microstructured surface was measured using H0. (b) The presence of concurrent hotspots decreased the hotspot dryout heat flux (blue, left ordinate), but increased the total heating power (red, right ordinate). (c) When the hotspot (H2) was superposed with a 10`W/cm$^2$ and 20`W/cm$^2$ uniform background heat flux, the hotspot dryout heat flux decreased (blue, left ordinate), but the total heating power increased (red, right ordinate).

## FURTHER READING

- I. Mudawar, "Assessment of High-heat-flux Thermal Management Schemes," *IEEE Trans. Compon. Packag. Technol.*, vol. 24, pp. 122-141, 2001.
- A. Bar-Cohen and P. Wang, "Thermal Management of On-chip Hot Spot," *J. Heat Transfer*, vol. 134, pp. 051017, 2012.
- J.-M. Koo, *et al*, "Integrated Microchannel Cooling for Three-dimensional Electronic Circuit Architectures," *J. Heat Transfer*, vol. 127, pp. 49-58, 2005.

# Prediction and Characterization of Dry-Out Heat Flux in Micropillar Wick Structures for Thermal Management Applications

Y. Zhu, D. S. Antao, Z. Lu, S. Somasundaram, T. J. Zhang, E. N. Wang

Sponsorship: ONR, Masdar Institute of Science and Technology, SMART

Thin-film evaporation in wick structures for cooling high-performance electronic devices is attractive because it harnesses the latent heat of vaporization and does not require external pumping. However, optimizing the wick structures to increase the dry-out heat flux is challenging due to the complexities in modeling the liquid–vapor interface and the flow through the wick structures. In this work, we developed a model for thin-film evaporation from micropillar array wick structures (Figure 1) and validated the model with experiments. The model numerically simulates liquid velocity, pressure, and meniscus curvature along the wicking direction by conservation of mass, momentum, and energy based on a finite volume approach. Specifically, the three-dimensional meniscus shape, which varies along the wicking direction with the local liquid pressure, is accurately captured by a force balance using the Young–Laplace equation. The dry-out condition is determined when the minimum contact angle on the pillar surface reaches the receding contact angle as the applied heat flux increases.

With this model, we predict the dry-out heat flux on various micropillar structure geometries (diameter, pitch, and height) in the length scale range of 1–100 µm and discuss the optimal geometries to maximize the dry-out heat flux (seen in Figure 2). We also performed detailed experiments to validate the model predictions, which all show good agreement. This work provides many insights into the role of surface structures in thin-film evaporation and also offers important design guidelines for enhanced thermal management of high-performance electronic devices.

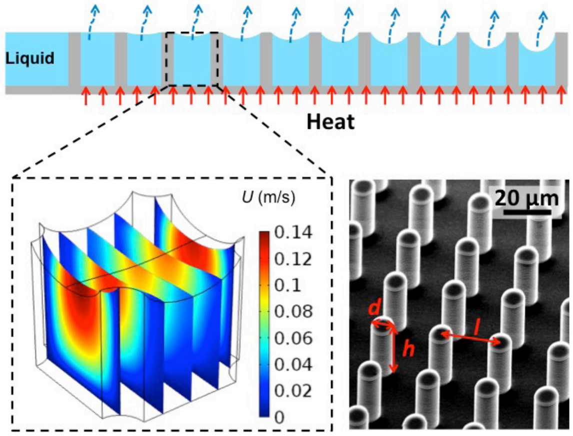

▲Figure 1: Side view schematic (top) of capillary-pumped liquid film that evaporates on a hydrophilic micropillar array surface, where a uniform heat flux is applied. The fluid velocity and liquid-vapor interface shape is solved in a unit cell (bottom left). A representative SEM image of a fabricated silicon micropillar array (bottom right) with diameter *d*, pitch *l*, and height *h*.

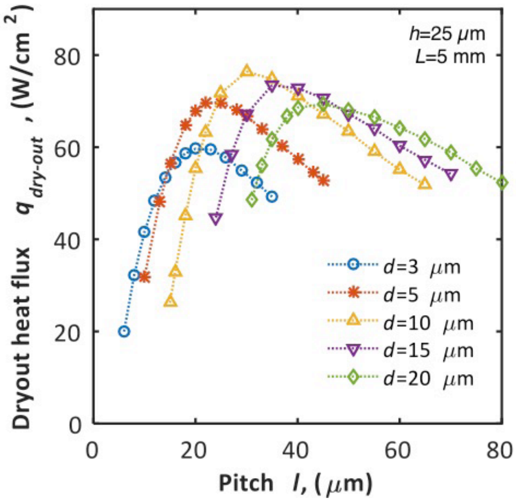

▲Figure 2: The dry-out heat flux $q_{dry\text{-}out}$ for various micropillar geometries. The micropillar height $h$ is 25 µm, and the receding contact angle of the evaporating liquid on the solid substrate is 15°.

## FURTHER READING

- Y. Zhu, D. S. Antao, Z. Lu, S. Somasundaram, T. J. Zhang, and E. N. Wang, "Prediction and Characterization of Dry-out Heat Flux in Micropillar Wick Structures," *Langmuir*, vol. 32, pp. 1920-1927, 2016.
- Y. Zhu, D. S. Antao, K. H. Chu, S. Chen, T. J. Hendricks, T. J. Zhang, and E. N. Wang, "Surface Structure Enhanced Microchannel Flow Boiling," *Journal of Heat Transfer*, vol. 138, pp. 091501, 2016.

# Enhanced Water Desalination in Electrochemical System

B. Kim, S. Choi, S. Ko, J. Han in collaboration with B. Al-Anzi, J. White, S. V. Pham
Sponsorship: Kuwait-MIT Center Signature Research Project / KFAS (Kuwait Foundation for the Advancement of Sciences)

Currently, reverse osmosis (RO) is considered the leading technology for desalination, and the operational efficiency of RO has been significantly improved over the last two decades with a thorough energy analysis. On the other hand, electrical desalination can be more advantageous in certain applications due to the diversity of allowed feed conditions, operational flexibility, and the relative low capital cost needed (the size of a system is generally small). Yet electrical desalination techniques such as electrodialysis (ED) have not been modeled in full detail, partially due to scientific challenges involving the multiphysics nature of the process. In addition, while current ED relies on bipolar ion conduction, removing one pair of a cation and an anion simultaneously, one final but most important point is that desalination achieved by means of an anion exchange membrane (AEM) and a cation exchange membrane (CEM) should be considered separately and independently (Figure 1a). Based on the intrinsically different ion transport near AEM and CEM, our group previously presented a novel process of ion concentration polarization (ICP) desalination (Figure 1b), which can basically enhance the amount of salt reduction, by examining unipolar ion conduction through both experiments and numerical modeling (Figure 1b). Since our experimental works are done in a model system for scalable electrochemical systems, the microfluidic device (Figure 1c) enables more scientific knowledge about ion transport phenomena through visualization. Meanwhile, the high-throughput module (stacked layer system, Figure 1d) enables us to realize a practical operation and evaluate the system's performance. Along with the ICP desalination, we also employed an ED system as a model to investigate the mass transport effects of embedded microstructures between the ion exchange membranes. In this work, therefore, we aim to perform a high-level analysis of ion transport near IEMs in order to enhance water desalination in electrochemical system.

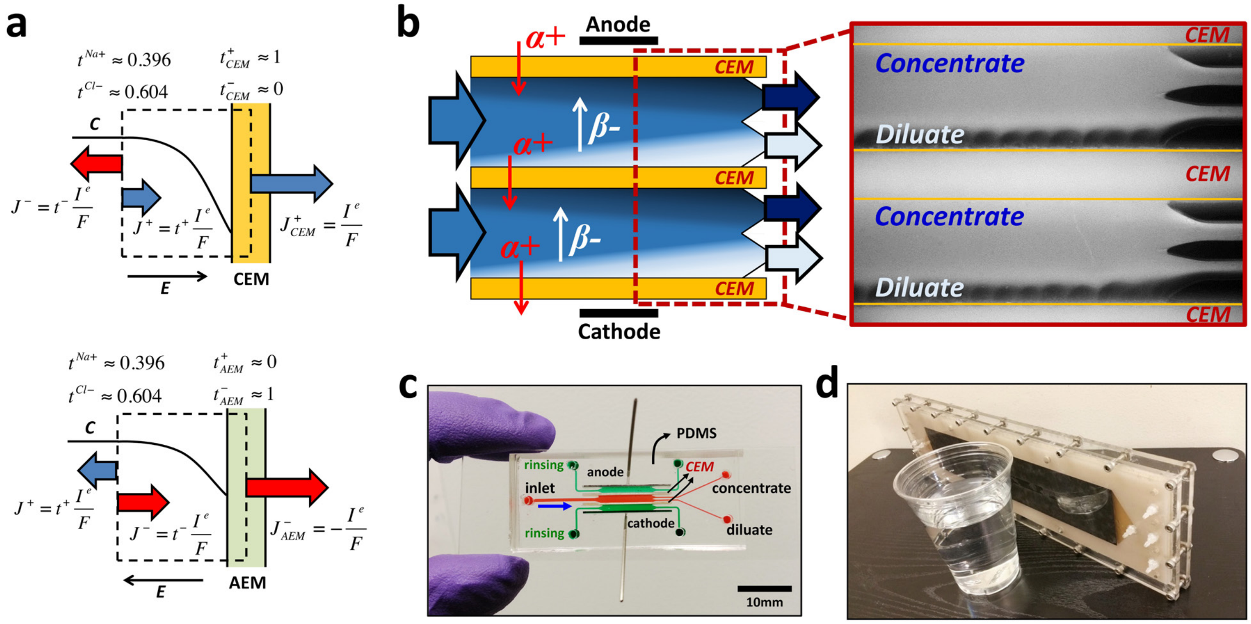

▲ Figure 1: Water desalination in electrochemical system; (a) Schematic diagram of counter-ion/co-ion transport near CEM/AEM, (b) schematics and fluorescent images of ICP desalination, photo of (c) microfluidic and (d) high-throughput devices.

## FURTHER READING

- R. Kwak, G. Guan, W. K. Peng, and J. Han, "Microscale Electrodialysis: Concentration Profiling and Vortex Visualization," *Desalination*, vol. 308, pp. 138-146, 2013.
- R. Kwak, V. S. Pham, B. Kim, L. Chen, and J. Han, "High-Throughput Salt/Bio-Agent Removal by Ion Concentration Polarization for Water Desalination," in *International Conference on Miniaturized Systems for Chemistry and Life Sciences*, pp. 660-662, 2013.
- B. Kim, R. Kwak, H. J. Kwon, V. S. Pham, S. E. Kooi, G. Lim, and J. Han, "Purification of Ultra-High Salinity Produced Water by Multi-Stage Ion Concentration Polarization," *International Conference on Miniaturized Systems for Chemistry and Life Sciences*, pp. 160-162, 2014.

# Fabrication of Core-Shell Microparticles Using 3-D Printed Microfluidics

D. Olvera-Trejo, L. F. Velásquez-García

Sponsorship: Tecnológico de Monterrey/MIT Nanotechnology Program

Coaxial electrospraying is an electrohydrodynamic process that creates core-shell microparticles by atomization of a coaxial electrified jet composed of two immiscible liquids. Coaxial electrospraying has several advantages over other microencapsulation technologies including higher encapsulation efficiency and more uniform size distribution. Coaxial electrosprayed compound microparticles can be used in exciting applications such as feedstock microencapsulation, controlled drug release, and self-healing composites.

Unlike traditional, i.e., uniaxial, electrospraying that has been investigated for over 100 years and of which many MEMS implementations exist, coaxial electrospraying was first described in 2002 and no microfabricated coaxial electrospray source had been reported due to the inherent three-dimensionality and complexity of its hydraulic system.

Stereolithography (SLA) is a layer-by-layer additive manufacturing process that creates solid objects via photopolymerization of a resin using ultraviolet light. Additive manufacturing started as a visualization tool for mesoscaled objects, but recent developments in the resolution and capabilities of 3-D printing suggest that these manufacturing processes could address the complexity, three-dimensionality, and material requirements of many microsystems. In particular, high-resolution SLA can be used to manufacture freeform microfluidics at a small fraction of the cost per device, infrastructure cost, and fabrication time of a typical silicon-based microfluidic system.

We developed SLA 3-D printed coaxial electrospray sources with one or two emitters that are fed by two helical channels (Figure 1). Each emitter spout is designed to produce a coaxial flow and to enhance the electric field on the liquid meniscus. Using these devices, we produced uniform core-shell microparticles using deionized water as the inner liquid and sesame oil as the outer liquid (Figure 2). The size of the droplets can be modulated by controlling the flow rates fed to the emitters. Electrical characterization of the devices demonstrates that the emitters operate uniformly. Current research efforts focus on demonstrating massively multiplexed sources with uniform array operation.

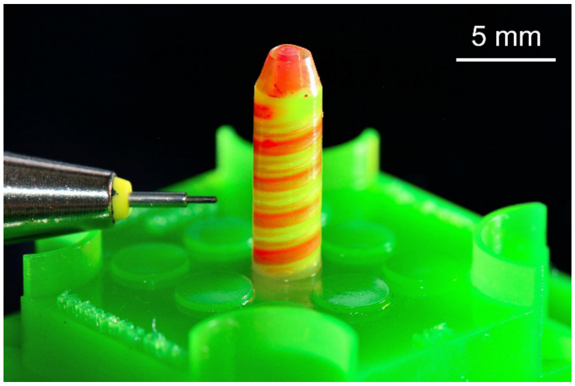

▲Figure 1: 3-D printed coaxial electrospray device next to a 0.3-mm-diameter mechanical pencil; the different colors of the liquids supplied to the device evidence the helical channels that feed the emitter nozzle.

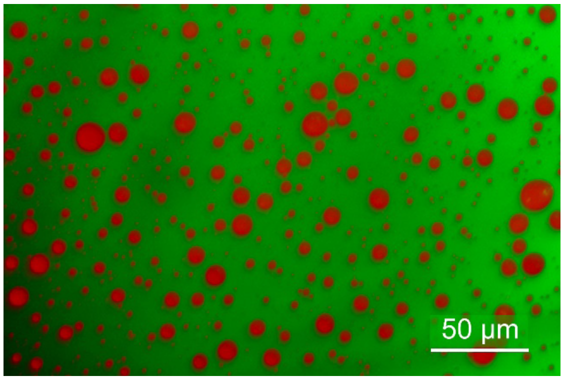

▲Figure 2: Optical image from a fluorescent microscope of core-shell droplets (core is water dyed with Rhodamine B, shell is sesame oil) immersed in water dyed with fluorescein. The compound particles were produced by one of our 3-D printed coaxial electrospray sources. The oil shell covering each red-colored core of the droplets prevents their mixing with green-colored water.

## FURTHER READING

- L. F. Velásquez-García, "SLA 3-D Printed Arrays of Miniaturized, Internally-fed, Polymer Electrospray Emitters," *Journal of Microelectromechanical Systems*, vol. 24, no. 6, pp. 2117-2127, December 2015.
- D. Olvera-Trejo and L. F. Velásquez-García, "3-D Printed Microfluidic Devices for Electrohydrodynamic Generation of Core-shell Microparticles," in *Technical Digest 17th Solid-State Sensor, Actuator and Microsystems Workshop*, pp. 176 – 179, 2016.

# 3-D Printed Massively Multiplexed Electrospray Sources

L. F. Velásquez-García
Sponsorship: U.S. Army

Electrospray is a electrohydrodynamic phenomenon that produces from a meniscus a stream of micro/nanoparticles that, depending on the properties of the liquid and the process conditions, can be droplets, ions, or fibers. The low spread in size and specific charge of the emitted particles makes the use of electrospray attractive in applications such as combustors, maskless micro/nanomanufacturing, and nanosatellite propulsion. However, the throughput of an electrospray emitter is very low, limiting the applicability of single-emitter electrospray sources to a few practical cases, e.g., mass spectrometry of biomolecules.

An approach to increase the throughput of an electrospray source without increasing the size variation of the emission is implementing arrays of electrospray emitters that operate in parallel. Miniaturization of the electrospray emitters results in less power consumption and lower onset voltage; in addition, using micro-fabrication, monolithic arrays of miniaturized emitters with large array size and emitter density can be made. Researchers have demonstrated a variety of MEMS multiplexed electrospray sources that operate uniformly. Although these devices work satisfactorily, they present a number of issues: (i) the device architecture is often a compromise between what should be made based on the modeling and what can be made given the limitations of traditional microfabrication, sacrificing device performance; (ii) a change in any of the in-plane features of the design requires the redesign and fabrication of one or more lithography masks while causing added costs and time delays; (iii) these devices are fairly expensive because they are made in a multimillion semiconductor-grade cleanroom with advanced tools that are operated by highly trained staff, which restricts their application to high-end applications and research.

We recently demonstrated the first 3-D printed multiplexed electrospray sources in the literature (Figure 1). The devices were fabricated with stereolithography and have associated two orders of magnitude less fabrication cost per device, fabrication time, and manufacturing infrastructure cost compared to a silicon MEMS multiplexed electrospray source. The 3-D printed devices include features not easily attainable with other microfabrication methods, e.g., tapered channels and threaded holes. Through the optimization of the fabrication process, arrays with as many as 236 internally fed electrospray emitters (236 emitters in 1 cm$^2$) were made, i.e., a twofold increase in emitter density and a sixfold increase in array size compared with the best reported values from multiplexed, internally fed, electrospray sources made of polymer. The characterization of devices with a different array size suggests a uniform emitter operation (Figure 2).

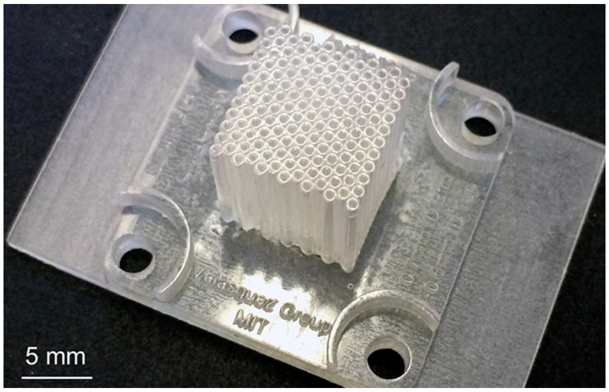

▲ Figure 1: A 3-D printed planar array of 143 tapered, internally fed electrospray emitters in 1 cm$^2$ (143 emitters/cm$^2$, hexagonal packing) The emitters are fed by 12 mm long tapered internal channels with 400 μm diameter at the emitter spouts.

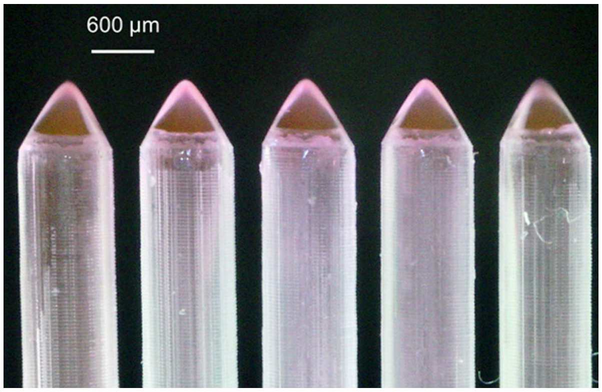

▲ Figure 2: External row of 5 emitters part of a 49-emitter planar array (70 emitters/cm$^2$, square packing). The scalloping on the exterior of the emitters, due to the layer-by-layer manufacturing, is visible.

## FURTHER READING

- B. Gassend, L. F. Velásquez-García, A. I. Akinwande, M. Martínez-Sánchez, "A Microfabricated Planar Electrospray Array Ionic Liquid Ion Source with Integrated Extractor," *J. Microelectromech. Syst.*, vol. 18, no. 3, pp. 679-694, June 2009.
- F. A. Hill, E. V. Heubel, P. J. Ponce de Leon, L. F. Velásquez-García, "High-Throughput Ionic Liquid Ion Sources Using Arrays of Microfabricated Electrospray Emitters with Integrated Extractor Grid and Carbon Nanotube Flow Control Structures," *J. Microelectromech. Syst.*, vol. 23, no. 5, pp. 1237-1248, October 2014.
- L. F. Velásquez-García, "SLA 3-D Printed Arrays of Miniaturized, Internally-fed, Polymer Electrospray Emitters," *J. Microelectromech. Syst.*, vol. 24, no. 6, pp. 2117 – 2127, December 2015.

# Optimization of Capillary Flow through Open Microstructured Arrays

P. Ponce de Leon, L. F. Velásquez-García
Sponsorship: DARPA

Liquid propagation through porous microstructures has received significant attention due to the importance of precisely controlling flow in microfluidic systems. Periodic surface structures, e.g., arrays of open micropillars or open microchannels, sometimes can be used to control the flow in a microsystem, introducing benefits such as direct access to the porous structure, device reusability, and resilience against clogging. In an open fluidic structure, the liquid is not actively pumped, e.g., using an upstream pressure signal; instead, the microstructured surface passively drives the liquid via capillary action. However, the same surfaces driving the flow via surface tension's pull simultaneously impede it by way of viscous resistance. Therefore, optimization of the geometry of the microstructured surface is required to maximize the flow rate it transports.

We developed semi-analytical models that describe the dynamics of capillary flow against gravity in (i) vertical arrays of open microchannels with rectangular cross-section and (ii) arrays of open micropillars with square packing and square cross section. We also extended our analysis to capture the shear-thinning behavior typical of many non-Newtonian fluids. Our models indicate the existence of multiple flow rate maxima with respect to pore size. One maximum, which occurs only in micropillar arrays, arises from the trade-off between capillary pressure and viscous resistance. The two other maxima, which occur for both micropillar and microchannel arrays, are related to meniscus and gravitational effects and only appear at low aspect-ratio (i.e., in channels/gaps between adjacent pillars that are about as wide as they are deep) and high Bond number, respectively. Experimental capillary rise data demonstrate that incorporating first-order gravitational effects and the impact of meniscus curvature improved flow rate predictions relative to models that neglect these factors (Figures 1 and 2; in both figures the working liquid is 1% PEO in 40/60 ethanol/water). Experimental capillary rise data also confirm the existence and location of a flow maximum with respect to the width of an open-microchannel; operating at any of the maxima decreases the sensitivity of flow rate to geometric variation, allowing for more robust microfluidic systems. Finally, we demonstrated electrospray emission from the edge of a microstructured surface as an example of an application of the porosity geometries we investigated in this study; the supply-limited regime of the current-voltage characteristics of these devices are in agreement with the literature on electrospray droplet emission, opening the possibility to implement arrays of externally-fed electrohydrodynamic jetting emitters that can operate continuously while producing droplets or nanofibers using suitable working liquids.

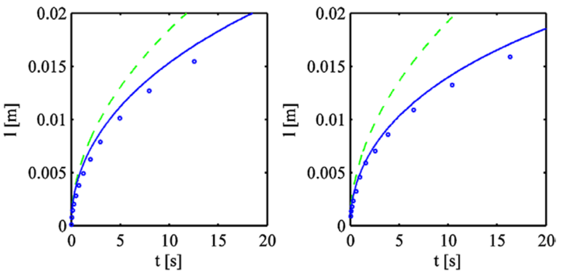

▲Figure 1: Height of rising liquid front vs. time for various open-microchannel geometries. In each subplot the blue circles are measured data points. The solid blue line shows the predictions of our model, and the dashed green line shows predictions neglecting gravitational and meniscus-permeability effects. Left – microchannels 139 µm deep, 149 µm wide, 101-µm thick walls; right – microchannels 141 µm deep, 211 µm wide, 289-µm thick walls.

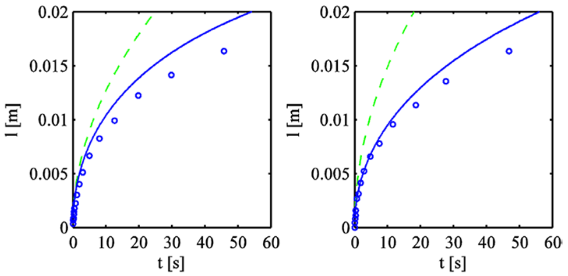

▲Figure 2: Height of rising liquid front vs. time for various open-micropillar array geometries. In each subplot the blue circles are measured data points, the solid blue line shows the predictions from our data, and the dashed green line shows predictions of the model proposed by Xiao *et al*, ***Langmuir***, 2010. Left – micropillars 140 µm tall, 93 µm wide, 157 µm gap; right – microchannels 143 µm tall, 289 µm wide, 211 µm gap.

## FURTHER READING

- F. A. Hill, E. V. Heubel, P. J. Ponce de Leon, and L. F. Velásquez-García, "High-throughput Ionic Liquid Ion Sources Using Arrays of Microfabricated Electrospray Emitters with Integrated Extractor Grid and Carbon Nanotube Flow Control Structures," *Journal of Microelectromech. Syst.*, vol. 23, no. 5, pp. 1237-1248, October 2014.
- P. J. Ponce de Leon, F. A. Hill, E. V. Heubel, and L. F. Velásquez-García, "Parallel Nanomanufacturing via Electrohydrodynamic Jetting From Microfabricated Externally-fed Emitter Arrays," *Nanotechnology,* vol. 26, no. 22, pp. 225301-1 – 225301-10, June 2015.
- P. J. Ponce de Leon, and L. F. Velásquez-García, "Optimization of Capillary Flow Through Open-microchannel and Open-micropillar Arrays," *Journal of Physics D – Applied Physics,* vol. 49, no. 5, pp. 055501-1 – 055501-13, February 2016.

# Chip-Scale Electrostatic Vacuum Ion Pump with Nanostructured Field Emission Electron Source

A. Basu, L. F. Velásquez-García
Sponsorship: DARPA

Cold-atom interferometry of alkali atoms can be used in a variety of high-precision sensors and timing devices such as atomic clocks, gyroscopes, accelerometers, magnetometers, and gravimeters. These devices require ultra-high vacuum (UHV, pressure < $10^{-9}$ Torr) to operate; therefore, chip-scale versions require miniaturized UHV pumps resilient to alkali metal vapors that consume power at levels compatible with device portability. In a macro-sized chamber, UHV-level vacuum can be maintained using a conventional magnetic ion pump, where electrons that swirl around the magnetic lines of a magnet create ions by impact ionization of neutral molecules, which in turn sputter a Ti getter. While scaled-down versions of magnetic ion pumps have been reported, these are incompatible with miniaturized cold-atom interferometry systems because (i) a reduction in the pump size increases the required threshold magnetic field for electron trapping, and (ii) the larger magnetic field associated with a miniaturized ion pump can interfere with the operation of the cold-atom sensor, yielding flawed readings. Non-evaporable getter (NEG) pumps are used in some cold-atom interferometry systems, e.g., commercial chip-scale atomic clocks; however, NEG pumps are unable to pump noble gases such as He and N2 that are present in the chamber, and they inefficiently pump alkali vapors.

We are developing vacuum ion pumps compatible with chip-scale cold-atom interferometry devices. The proposed field emitter array (FEA)-based magnet-free ion pump architecture is shown in Figure 1. In this pump design, a helical electron collector pulls the electrons toward itself, forcing them to first travel beyond the height of the electron collector, to then get pushed back due to the electrostatic mirror effect of the annular-shaped ion collector. Therefore, the trajectory of the electrons is significantly increased compared to a pump design with a parallel-capacitor electrode configuration, augmenting the probability of impact ionization. The FEA consists of arrays nano-sharp silicon tips, each surrounded by a self-aligned gate electrode; we have shown that these FEAs do not degrade in the presence of Rb vapor.

Figure 2 shows the semi-log plot of the minus time derivative of the pressure versus time during pump-down, with the horizontal axis denoting the time since the beginning of each pump-down cycle; in these experiments, the pressure inside the chamber reached values as low as ~$7 \times 10^{-7}$ Torr. Each data point in the plot represents an average of the minus time derivative of the pressure considering all pump-down cycles. The $R^2$ of the linear fit of the data evidences that our reduced-order model accurately explains the dynamics of the pump. The slope of the linear fit of the data estimates the experimental pumping time constant at about 161 seconds.

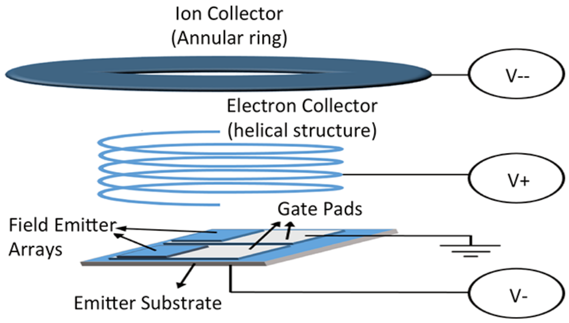

▲Figure 1: Schematic of the FEA-based, magnetic-less ion pump architecture.

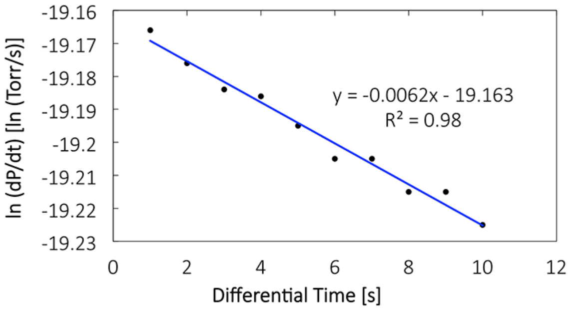

▲Figure 2: Semi-log plot of the negative of the time derivative of the chamber pressure vs. time. From the slope of the linear fit, τ = 161.2 s.

## FURTHER READING

- A. Basu, M. A. Perez, and L. F. Velásquez-García, "Nanostructured Silicon Field Emitter Array-based High-vacuum Magnetic-less Ion Pump for Miniaturized Atomic Spectroscopy Sensors," *Technical Digest of the 18th International Conference on Solid-State Sensors, Actuators, and Microsystems (Transducers 2015)*, Anchorage AK, pp. 1021-1024, June 2015.
- A. Basu, M. A. Perez, and L. F. Velásquez-García, "Miniaturized, Electrostatic, High-vacuum Ion Pump Using a Nanostructured Field Emission Electron Source," *15th International Conference on Micro and Nanotechnology for Power Generation and Energy Conversion Applications (PowerMEMS 2015)*, Boston, MA, December 2015; *Journal of Physics Conference Series*, vol. 660 pp. 012027-1 – 012027-5, 2015.
- A. Basu and L. F. Velásquez-García, "Electrostatic Ion Pump with Nanostructured Si Field Emission Electron Source and Ti Particle Collectors for Supporting Ultra-high Vacuum in Miniaturized Atom Interferometry Systems," *Journal of Micromechanics and Microengineering*, 2016.